

Electromagnetic radii of the nucleon in soft-wall holographic QCD

Kiminad A. Mamo*

Physics Division, Argonne National Laboratory, Argonne, Illinois 60439, USA

Ismail Zahed†

*Center for Nuclear Theory, Department of Physics and Astronomy,
Stony Brook University, Stony Brook, New York 11794-3800, USA*

(Dated: April 20, 2022)

We revisit the electromagnetic form factors of the proton and neutron in the original-minimal soft-wall holographic QCD, which has only two parameters, i.e., the mass scale κ and the twist parameter of the nucleon τ . We first fix $\tau = 3$ by the hard scattering rule, and extract $\kappa = 0.402$ GeV from the world data (including the Mainz A1 data) of the Sachs magnetic form factor of the proton G_M^p . We then predict among others, the charge radius of the proton to be $r_p = 0.831 \pm 0.008$ fm, in perfect agreement with the recent charge radius of the proton measured by the PRad collaboration at Jefferson Lab, and in agreement with the muonic hydrogen experiments. Our prediction for the proton elastic form factor ratio $\mu_p G_E^p / G_M^p$ is also in very good agreement with the recent high precision Jefferson Lab recoil polarization experiment E08-007 for $Q^2 = 0.3 - 0.6$ GeV², and with the recent high precision Mainz A1 experiment for $Q^2 < 0.13$ GeV².

PACS numbers:

I. INTRODUCTION

The nucleon is a composite hadron with quarks and gluons constituents, the stuff at the origin of all hadronic matter. The quarks are charged and their distribution inside a nucleon is captured by the electric and magnetic charge radii, which measure the charge and current distributions respectively. Precision electron scattering and spectroscopic measurements show a stubborn 4% discrepancy, the so-called proton radius puzzle [1–4]. This is a surprising state of affairs given the fundamental nature of the proton.

The proton structure is the quintessential QCD problem, currently addressed using ab-initio lattice simulations [5]. Empirically, the mass of the proton is known with great accuracy, but its fundamental charge radius is not, as shown in Fig. 1. The high precision elastic e-p scattering measurement of 0.879 fm by Mainz A1 collaboration [6] while consistent with the value of 0.877 fm from the previous hydrogen spectroscopy [7], is larger than the reported value of 0.841 fm from muonic hydrogen spectroscopy [8], and the values of 0.833 fm and 0.848 fm from the recent hydrogen spectroscopy measurements [9, 10]. Moreover, the newest e-p measurement by the PRad collaboration at Jefferson Lab has reported a small charge radius of 0.831 fm [11]. A smaller charge radius is also supported by various re-analysis of the Mainz A1 e-p scattering data [12–17] with few exceptions [18, 19]. In addition, the recent combined re-analysis of the Mainz A1 and PRad data has also favored a small charge radius [20–24].

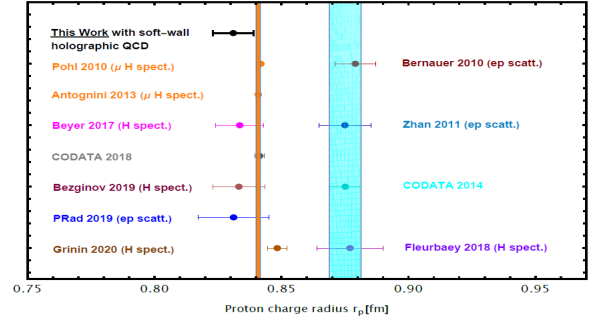


FIG. 1: World data for the proton charge radius. The black dot (with its theoretical error bar) is our prediction within the original-minimal soft-wall holographic QCD [25] with $\tau = 3$ and $\kappa = 0.402$ GeV, see Table I. The dark-yellow dot is the prediction of Abidin and Carlson [26] (which is also within the original-minimal soft-wall holographic QCD [25] with $\tau = 3$ and $\kappa = 0.350$ GeV), see also Table I. The other dots are the world experimental data for the proton charge radius Pohl 2010 (μ H spect.) [27], Antognini 2013 (μ H spect.) [8], Beyer 2017 (H spect.) [28], CODATA 2018 [29], Beznin 2019 (H spect.) [9], PRad 2019 (ep scatt.) [11], Grinin 2020 (H spect.) [10], Bernauer 2010 (ep scatt.) [6], Zhan 2011 (ep scatt.) [30], CODATA 2014 [31], and Fleurbaey 2018 (H spect.) [7].

All in all, tension seems to exist between e-p scattering measurements of the proton charge radius, and atomic measurements using muonic hydrogen as illustrated in Fig. 1. Although ideas beyond the standard model have been suggested to fix the discrepancy [32, 33], none so far has been empirically conclusive.

The proton structure emerges from a subtle interplay between the sources composing the nucleon and the primordial glue in the vacuum [34]. Most of the proton mass arises from the primordial and topological glue at the origin of the spontaneous breaking of chiral symmetry, but

*Electronic address: kmamo@anl.gov

†Electronic address: ismail.zahed@stonybrook.edu

its moderately large size makes it still susceptible to the effects of confinement. This last feature is also shared by the vector mesons, but not the light and more compact pseudoscalar Goldstone bosons. This last observation is further supported by the straight character of the nucleon and rho Regge trajectories, and their remarkable parallelism.

We will address the proton and neutron size problem non-perturbatively in the context of holographic QCD, which among other embodies Regge physics, and provides a field theoretical realization for the dual resonance framework [35] postulated decades ago outside the realm of QCD. It is the most economical way of enforcing basic symmetries, including crossing symmetry and unitarity, the key tenets in dispersive analyses. The approach, originates from a conjecture that observables in strongly coupled and conformal gauge theories in the limit of a large number of colors and strong gauge coupling, can be determined from classical fields interacting through gravity, in an anti-de-Sitter space in higher dimensions [36, 37]. The conjecture has been extended since to non-conformal gauge theories [25, 38].

The holographic description of the electromagnetic form factors in the context of the original-minimal soft-wall holographic QCD [25] was initially addressed in [26] (with just two parameters, the mass scale κ and twist of proton τ) with rather large electromagnetic radii for $\kappa = 0.350$ GeV (fixed by simultaneously fitting the holographic mass of the rho meson and proton to their experimental values, see Table I), and $\tau = 3$ (fixed by the hard scattering rule). Here we show how to overcome this major shortcoming by fixing $\kappa = 0.402$ GeV (fixed by fitting the holographic Sachs magnetic form factor of the proton to the world data (including the Mainz A1 data) of the Sachs magnetic form factor of proton), see Table I, and Fig. 2. We also fix $\kappa = m_\rho/2 = 0.388$ GeV, and $\tau = m_N^2/m_\rho^2 + 1 = 2.465$ at low energy, assuming that

the nucleon anomalous dimension or the twist τ , runs with the energy scale to asymptote its hard scaling value $\tau = 3$ at high energy [39], see Table I. The difference between these two choices of the holographic parameters κ and τ , will help us estimate our theoretical uncertainty in determining the electromagnetic radii of the nucleons.

The organization of the paper is as follows: in section II, we write down the holographic Sachs electric and magnetic form factor of the nucleon which are derived in detail, within the original-minimal holographic QCD [25, 26]. In section III, we show the three possible ways of fixing the only two parameters κ and τ of the original-minimal holographic QCD, and summarize the corresponding predictions for the charge radius of the proton in Table I. Finally, in section IV, we compute the charge and magnetic radii of both the proton and neutron, and compare the holographic predictions, within the theoretical uncertainties, to the experimental values. We also summarize our results in Table II. Our conclusions are in V. More details can be found in the Appendices.

II. NUCLEON ELECTRIC AND MAGNETIC SACHS FORM FACTORS

We define the standard electric and magnetic Sachs form factors of the proton and neutron as

$$G_E^{P,N}(Q) = F_1^{P,N}(Q) - \frac{Q^2}{4m_N^2} F_2^{P,N}(Q), \quad (\text{II.1})$$

$$G_M^{P,N}(Q) = F_1^{P,N}(Q) + F_2^{P,N}(Q), \quad (\text{II.2})$$

where the Dirac $F_1(Q)$ and Pauli $F_2(Q)$ form factors of proton (P) and neutron (N) in the original-minimal soft-wall holographic QCD [25] are given by (see the Appendix for their detailed derivation, see also [26, 40])

$$F_1^P(Q) = \left(\frac{a}{2} + \tau\right) \times B(\tau, a+1) + \eta_P \times (\tau-1) \times \frac{a(a(\tau-1)-1)}{(a+\tau)(a+\tau+1)} \times B(\tau-1, a+1), \quad (\text{II.3})$$

$$F_2^P(Q) = \eta_P \times 4(\tau-1) \times \tau \times B(\tau, a+1), \quad (\text{II.4})$$

$$F_1^N(Q) = \eta_N \times (\tau-1) \times \frac{a(a(\tau-1)-1)}{(a+\tau+1)(a+\tau)} \times B(\tau-1, a+1), \quad (\text{II.5})$$

$$F_2^N(Q) = \eta_N \times 4(\tau-1) \times \tau \times B(\tau, a+1), \quad (\text{II.6})$$

Here we have defined $a = Q^2/4\kappa^2$ with $Q^2 = -q^2 \leq 0$, and denoted by κ the mass scale, τ the twist parameter of the nucleon, and by $B(x, y) = \Gamma(x)\Gamma(y)/\Gamma(x+y)$ the Euler beta function. The additional coefficients $\eta_{P,N} = 2g_5^2 \times (\eta_3 \pm \eta_0)/2$ in (II.3-II.6) follow from the extra couplings $\eta_{0,3}$, for the singlet and triplet contributions of the bulk Pauli contribution [26].

The Pauli parameter of the proton η_P can be determined by matching the value of $F_2^P(0)$ with the experimental data which is 1.793, i.e.

$$\eta_P = \frac{1.793}{C_3(0)} = \frac{1.793}{4(\tau-1)}. \quad (\text{II.7})$$

Similarly, the Pauli parameter of the neutron η_N can be determined by matching the value of $F_2^N(0)$ with the

experimental data which is -1.913 , i.e.

$$\eta_N = \frac{-1.913}{C_3(0)} = \frac{-1.913}{4(\tau - 1)}. \quad (\text{II.8})$$

Soft-wall AdS/QCD	κ	τ	$m_\rho^2 = 4\kappa^2$	$m_N^2 = 4\kappa^2(\tau - 1)$	$\sqrt{\langle r_C^p \rangle^2}$
This Work	0.388 GeV	2.465	0.775^2 GeV^2 (exp.)	0.938^2 GeV^2 (exp.)	0.839 fm (pr.)
This Work	0.402 GeV	3.000	0.804^2 GeV^2 (pr.)	1.137^2 GeV^2 (pr.)	0.831 fm (pr.)
Abidin-Carlson [26]	0.350 GeV	3.000	0.700^2 GeV^2 (pr.)	0.990^2 GeV^2 (pr.)	0.960 fm (pr.)

TABLE I: Comparison of the values of the holographic parameters (κ and τ), and the corresponding predictions for the charge radius of the proton $\sqrt{\langle r_C^p \rangle^2}$ in our work (see (IV.14-IV.15)) within the original-minimal soft-wall holographic QCD [25], and the work of Abidin and Carlson [26] (which is also within the original-minimal soft-wall holographic QCD [25]). Note that **pr.** and **exp.** are shorthand for the **predicted** and **experimental** values, respectively.

III. FIXING THE MASS SCALE κ AND TWIST τ , IN THE ORIGINAL-MINIMAL SOFT-WALL HOLOGRAPHIC QCD

In this work, we first fix the twist parameter of the proton $\tau = 3$, to match the hard counting rule in the large Q^2 regime (see Appendix C for more details). We then fix the mass scale $\kappa = 0.402 \text{ GeV}$ by fitting the holographic Sachs magnetic form factor $G_M^P(Q)$ (II.2), to the world experimental data (including the Mainz A1 data) on the Sachs magnetic form factor, see Table I, and the solid-black curves in Fig. 2-4.

In this work, we also fix κ , as was done in the original-minimal soft-wall holographic QCD [25], by the mass of the ρ meson using the relation $4\kappa^2 = m_\rho^2$. Then, we fix τ by the mass of the nucleon using the relation $m_N^2 = 4\kappa^2(\tau - 1)$. Therefore, for $m_\rho = 0.775 \text{ GeV}$ and $m_N = 0.938$, we find $\tau = m_N^2/m_\rho^2 + 1 = 2.465$ and $\kappa = m_\rho/2 = 0.388 \text{ GeV}$, see Table I, and the solid-green curves in Fig. 2-4.

Our choice is in contrast to the earlier work of Abidin and Carlson [26], within the original-minimal soft-wall holographic QCD [25], where they first fixed $\tau = 3$ to match the hard counting rule in the large Q^2 regime, and then fixed $\kappa = 0.350 \text{ GeV}$ (by simultaneously fitting to the experimental mass of the rho meson and proton) which gives a smaller $m_\rho = 2\kappa = 0.700 \text{ GeV}$, and a larger mass of the nucleon $m_N = 2\kappa\sqrt{\tau - 1} = 0.990 \text{ GeV}$, see Table I, and the dark-yellow-solid curves in Figs. 2-4.

In Fig. 2, we show the magnetic Sachs form factor of the proton. The black-solid curve is our soft-wall holographic QCD result with $\tau = 3$ and $\kappa = 0.402 \text{ GeV}$. The green-solid curve is our soft-wall holographic QCD result with $\tau = m_N^2/m_\rho^2 + 1 = 2.465$ and $4\kappa^2 = m_\rho^2 = 0.775^2 \text{ GeV}^2$. The dark-yellow-solid curve

is the soft-wall holographic QCD result for $\tau = 3$ and $\kappa = 0.350 \text{ GeV}$ [26]. The solid-red curve is the Arrington fit to world data (without the Mainz A1 data) [41] (brown data points). The magenta data points are the Mainz A1 data [42]. Throughout, we have used the proton magnetic moment $\mu_p = G_M^P(0) = F_1^P(0) + F_2^P(0) = 2.793$.

In Fig. 3, we show the ratio of the Sachs electric and magnetic form factor of the proton at high and low momentum transfer. The black-solid curve is our soft-wall holographic QCD result with $\tau = 3$ (fixed by the hard counting rule) and $\kappa = 0.402 \text{ GeV}$ (extracted from the best fit to the world data (including Mainz A1 data) of Sachs magnetic form factor of proton). The green-solid curve is our soft-wall holographic QCD result with $\tau = m_N^2/m_\rho^2 + 1 = 2.465$ and $4\kappa^2 = m_\rho^2 = 0.775^2 \text{ GeV}^2$. The dark-yellow-solid curve is the soft-wall holographic QCD result for $\tau = 3$ and $\kappa = 0.350 \text{ GeV}$ [26]. The solid-red curve is the Arrington fit [41] to the world data (brown data points) (note that the world data (brown data points) is without the Mainz A1 [42] and the recent JLab recoil polarization experimental data [30, 43]). The magenta data points are the Mainz A1 data [42]. The two cyan data points are from the recent high precision JLab recoil polarization experiment E03-104 [43]. The dark-blue data points are from the recent high precision JLab recoil polarization experiment E08-007 [30].

In Fig. 4, we show the electric Sachs form factor of the proton. The black-solid curve is our soft-wall holographic QCD result with $\tau = 3$ and $\kappa = 0.402 \text{ GeV}$ (fixed using the world data of magnetic Sachs form factor of proton). The green-solid curve is our soft-wall holographic QCD result with $\tau = m_N^2/m_\rho^2 + 1 = 2.465$ and $4\kappa^2 = m_\rho^2 = 0.775^2 \text{ GeV}^2$. The dark-yellow-solid curve is the soft-wall holographic QCD result for $\tau = 3$ and $\kappa = 0.350 \text{ GeV}$ [26]. The solid-blue curve is the PRad fit

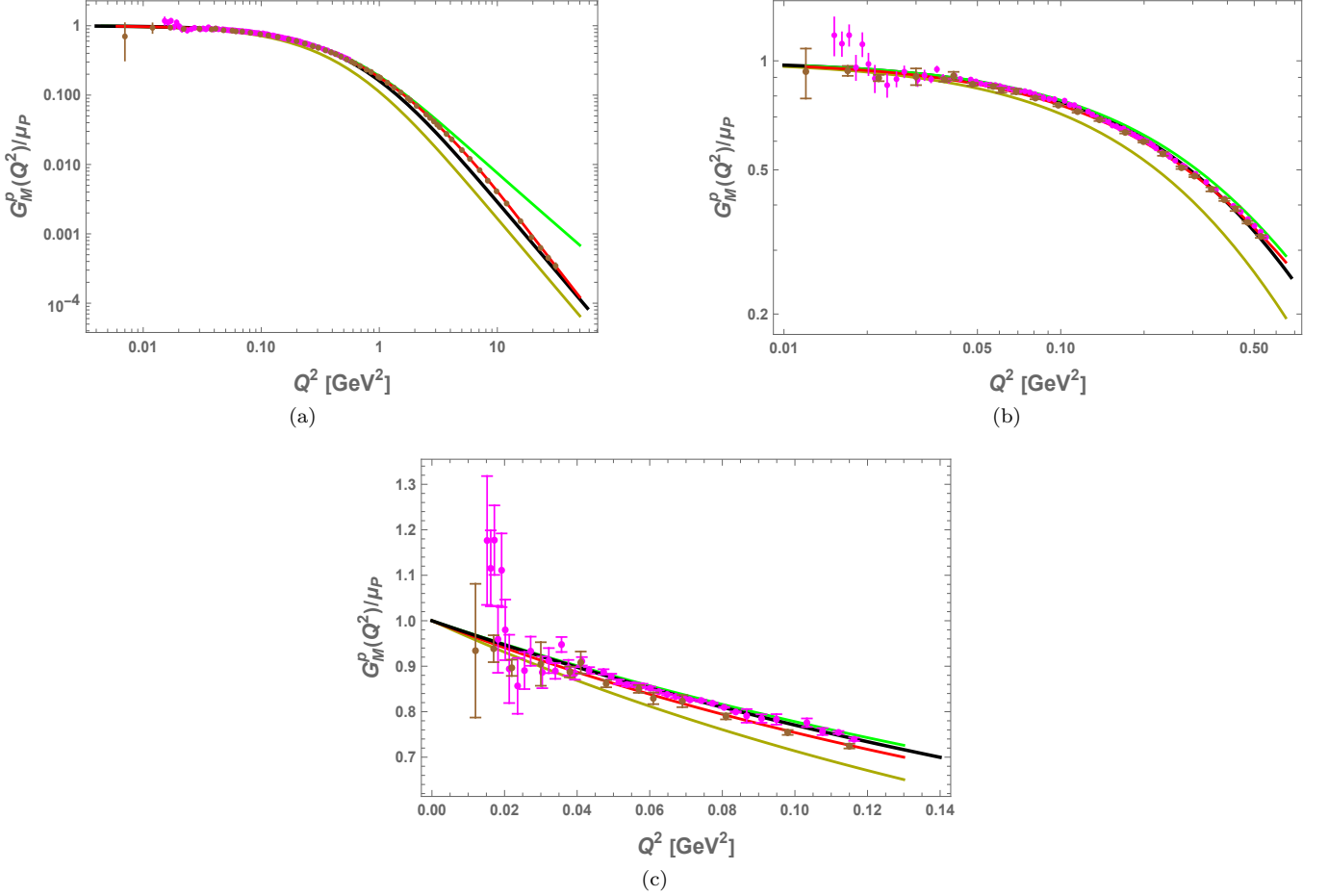


FIG. 2: Sachs magnetic form factor of the proton at high and low momentum transfer. The black-solid curve is our soft-wall holographic QCD result with $\tau = 3$ (fixed by the hard counting rule) and $\kappa = 0.402 \text{ GeV}$ (extracted from the best fit to the world data (including Mainz A1 data) of Sachs magnetic form factor of proton). The green-solid curve is our soft-wall holographic QCD result with $\tau = m_N^2/m_\rho^2 + 1 = 2.465$ and $4\kappa^2 = m_\rho^2 = 0.775^2 \text{ GeV}^2$. The dark-yellow-solid curve is the soft-wall holographic QCD result for $\tau = 3$ and $\kappa = 0.350 \text{ GeV}$ [26]. The solid-red curve is the Arrington fit to world data (without Mainz A1 data) [41] (brown data points). The magenta data points are the Mainz A1 data [42]. Throughout, we have used the proton magnetic moment $\mu_p = G_M^p(0) = F_1^p(0) + F_2^p(0) = 2.793$.

to PRad data [11] (orange and gray data points). The solid-red curve is the Arrington fit to world data (without PRad and Mainz A1 data) [41] (brown data points). The magenta data points are the Mainz A1 data [42]. Note that our holographic prediction (solid-black curve) completely overlaps with the PRad fit to the PRad data (solid-blue curve) in Fig. 4.c for $Q^2 < 0.006$.

IV. ELECTROMAGNETIC RADII

A. Proton

The magnetic radius of the proton is defined as

$$\langle r_M^2 \rangle_p = -6 \left(\frac{d \ln G_M^p(Q)}{dQ^2} \right)_0 \hbar^2 c^2, \quad (\text{IV.9})$$

with $\hbar c = 0.197 \text{ GeV fm}$. Using (II.2) in (IV.9), we find

$$\langle r_M^2 \rangle_p = (0.803 \text{ fm})^2 \quad (\text{extracted from world data}), \quad (\text{IV.10})$$

with $\kappa = 0.402 \text{ GeV}$ (fixed using the world data (including the Mainz A1 data) of the magnetic Sachs form factor of the proton, see Fig. 2), and $\tau = 3$ (fixed by the hard scattering rule). Alternatively, we have

$$\langle r_M^2 \rangle_p = (0.791 \text{ fm})^2, \quad (\text{IV.11})$$

for $\kappa = m_\rho/2 = 0.388 \text{ GeV}$, and $\tau = m_N^2/m_\rho^2 + 1 = 2.465$. Combining (IV.10) and (IV.11), we find our final magnetic radius of the proton

$$\langle r_M^2 \rangle_p = (0.803 \pm 0.012 \text{ fm})^2 \quad (\text{extracted from world data}), \quad (\text{IV.12})$$

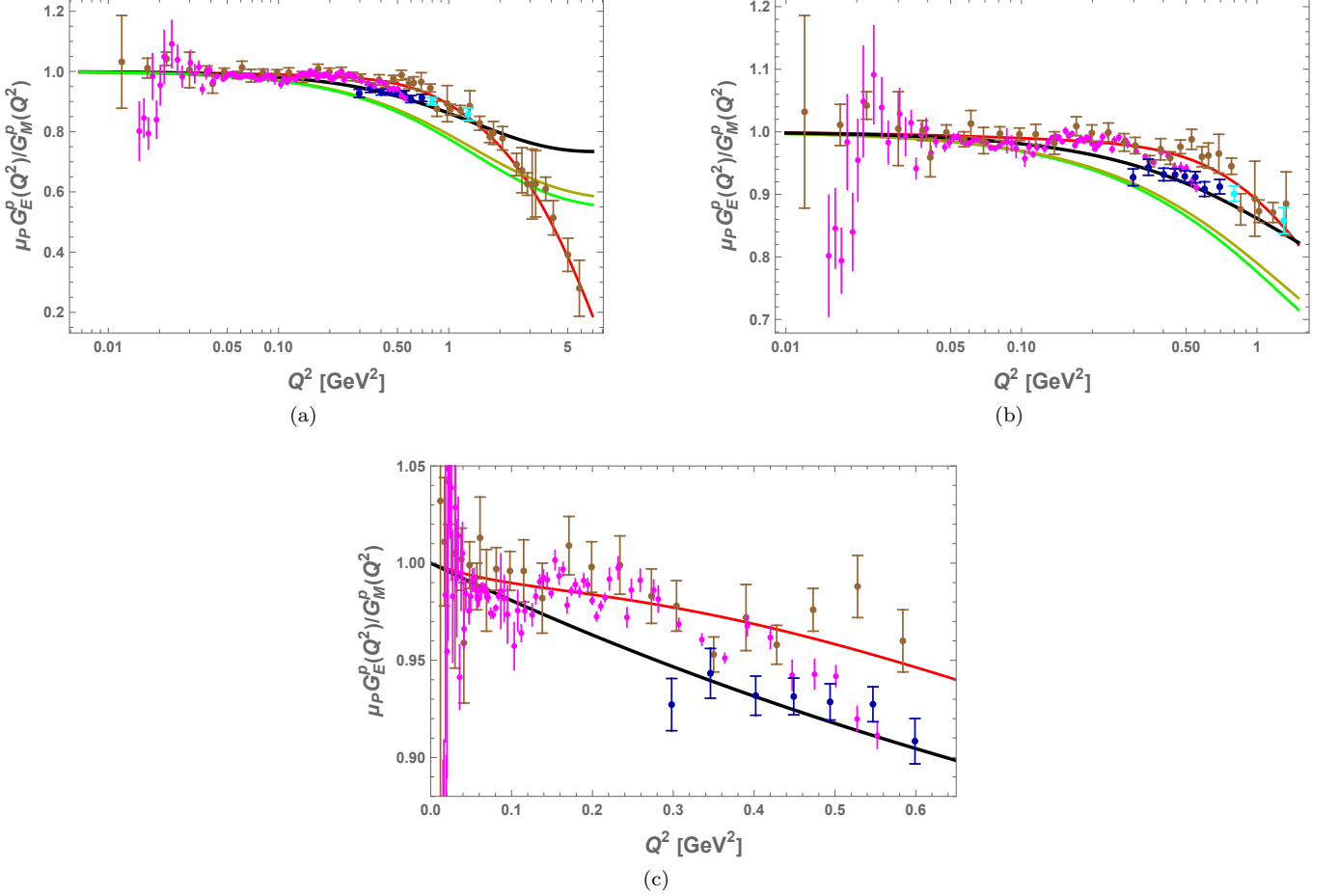


FIG. 3: The ratio of the Sachs electric and magnetic form factor of the proton at high and low momentum transfer. The black-solid curve is our soft-wall holographic QCD result with $\tau = 3$ (fixed by the hard counting rule) and $\kappa = 0.402$ GeV (extracted from the best fit to the world data (including Mainz A1 data) of Sachs magnetic form factor of proton). The green-solid curve is our soft-wall holographic QCD result with $\tau = m_N^2/m_\rho^2 + 1 = 2.465$ and $4\kappa^2 = m_\rho^2 = 0.775^2$ GeV². The dark-yellow-solid curve is the soft-wall holographic QCD result for $\tau = 3$ and $\kappa = 0.350$ GeV [26]. The solid-red curve is the Arrington fit [41] to the world data (brown data points) (note that the world data (brown data points) is without the Mainz A1 [42] and the recent JLab recoil polarization experimental data [30, 43]). The magenta data points are the Mainz A1 data [42]. The two cyan data points are from the recent high precision JLab recoil polarization experiment E03-104 [43]. The dark-blue data points are from the recent high precision JLab recoil polarization experiment E08-007 [30]. Throughout, we have used the proton magnetic moment $\mu_p = G_M^P(0) = F_1^P(0) + F_2^P(0) = 2.793$.

in good agreement with the average of e-p scattering Mainz A1 data (with the average of the most flexible Spline and Polynomial fits) [42], and world data (with Arrington and Sick (2015) world updated value [44] or equivalently with the extraction of Zhan, et al. (2011) [30]), respectively, which is $\langle r_M^2 \rangle_p^{\frac{1}{2}} = (0.777 \text{ fm} + 0.867 \text{ fm})/2 = 0.822 \text{ fm}$.

The charge radius of the proton is given by

$$\langle r_C^2 \rangle_p = -6 \left(\frac{d \ln G_E^P(Q)}{dQ^2} \right)_0 \hbar^2 c^2. \quad (\text{IV.13})$$

Using (II.1) in (IV.13), we find

$$\langle r_C^2 \rangle_p = (0.831 \text{ fm})^2, \quad (\text{IV.14})$$

for $\kappa=0.402$ GeV, and $\tau = 3$, see Table I-II. We also find

$$\langle r_C^2 \rangle_p = (0.839 \text{ fm})^2, \quad (\text{IV.15})$$

for $\kappa=0.388$ GeV, and $\tau = 2.465$, see Table I. Combining (IV.14) and (IV.15), we find our final charge radius of the proton

$$\langle r_C^2 \rangle_p = (0.831 \pm 0.008 \text{ fm})^2 \text{ (prediction)}, \quad (\text{IV.16})$$

see Fig. 1.

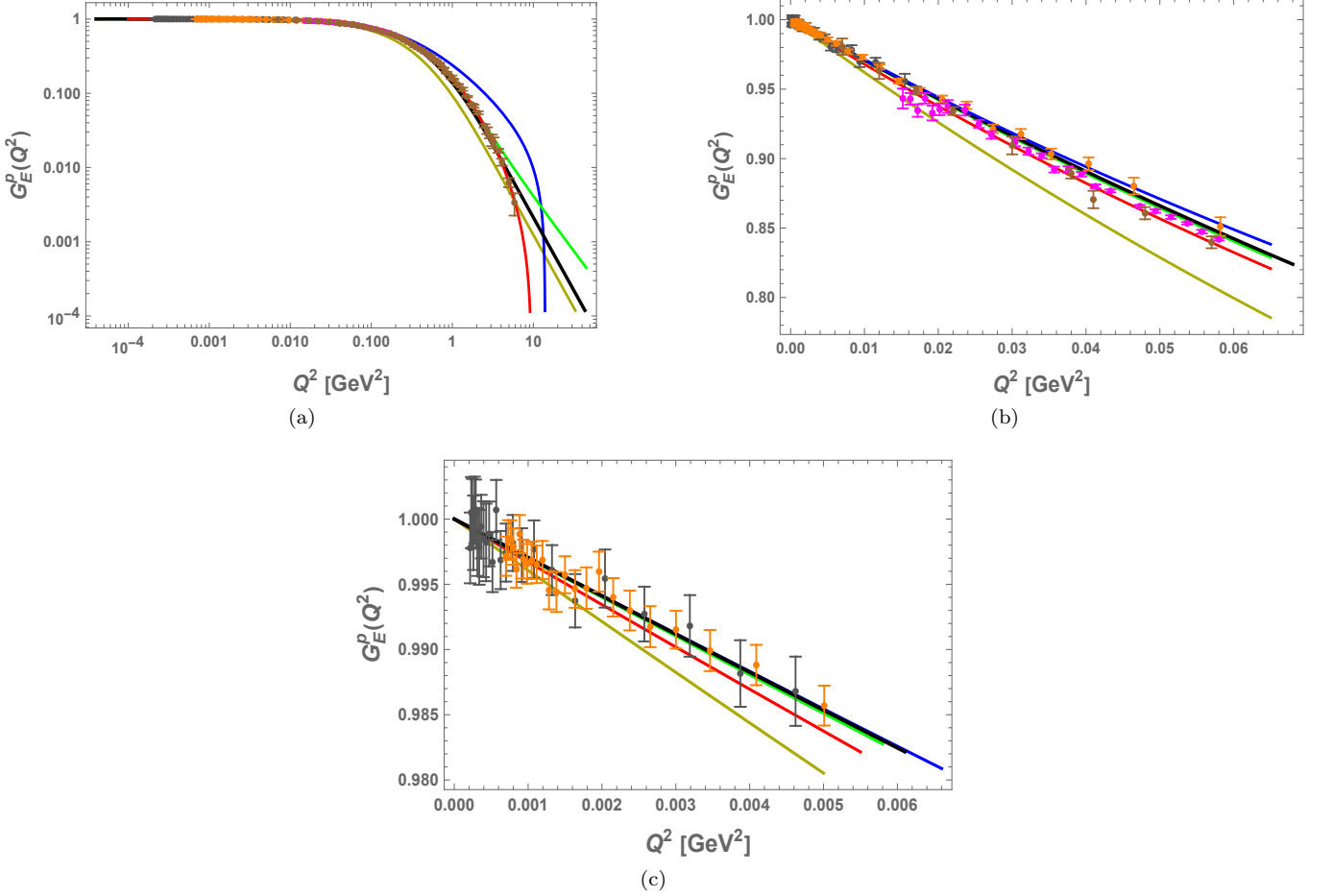


FIG. 4: Sachs electric form factor of the proton at high and low momentum transfer. The black-solid curve is our soft-wall holographic QCD result with $\tau = 3$ and $\kappa = 0.402 \text{ GeV}$. The green-solid curve is our soft-wall holographic QCD result with $\tau = m_N^2/m_\rho^2 + 1 = 2.465$ and $4\kappa^2 = m_\rho^2 = 0.775^2 \text{ GeV}^2$. The dark-yellow-solid curve is the soft-wall holographic QCD result for $\tau = 3$ and $\kappa = 0.350 \text{ GeV}$ [26]. The solid-blue curve is the PRad fit to PRad data [11] (orange and gray data points). The solid-red curve is the Arrington fit to world data (without PRad and Mainz A1 data) [41] (brown data points). The magenta data points are the Mainz A1 data [42]. Note that in (c) our holographic prediction (solid-black curve) completely overlaps with the PRad fit to PRad data (solid-blue curve).

B. Neutron

The magnetic radius of the neutron is defined as

$$\langle r_M^2 \rangle_n = -6 \left(\frac{d \ln G_M^N(Q)}{dQ^2} \right)_0 \hbar^2 c^2. \quad (\text{IV.17})$$

Using (II.2) in (IV.9), we find

$$\langle r_M^2 \rangle_n = (0.817 \text{ fm})^2, \quad (\text{IV.18})$$

with $\kappa = 0.402 \text{ GeV}$, and $\tau = 3$. We also find

$$\langle r_M^2 \rangle_n = (0.810 \text{ fm})^2, \quad (\text{IV.19})$$

for $\kappa = 0.388 \text{ GeV}$, and $\tau = 2.465$. Combining (IV.18) and (IV.19), we find our final magnetic radius of the neutron

$$\langle r_M^2 \rangle_n = (0.817 \pm 0.007 \text{ fm})^2 \text{ (prediction)}, \quad (\text{IV.20})$$

in good agreement with the PDG world average [45]

$$\langle r_M^2 \rangle_n^{\frac{1}{2}} = 0.864 \text{ fm}.$$

The charge radius of the neutron is given by

$$\langle r_C^2 \rangle_n = -6 \left(\frac{d G_E^N(Q)}{dQ^2} \right)_0 \hbar^2 c^2. \quad (\text{IV.21})$$

Using (II.1) in (IV.21), we find

$$\langle r_C^2 \rangle_n = (-0.094 \text{ fm})^2, \quad (\text{IV.22})$$

for $\kappa = 0.402 \text{ GeV}$, and $\tau = 3$. We also find

$$\langle r_C^2 \rangle_n = (-0.142 \text{ fm})^2, \quad (\text{IV.23})$$

for $\kappa = 0.388 \text{ GeV}$, and $\tau = 2.465$. Combining (IV.22) and (IV.23), we find our final charge radius of the neutron

$$\langle r_C^2 \rangle_n = (-0.094 \pm 0.048 \text{ fm})^2 \text{ (prediction)}. \quad (\text{IV.24})$$

in good agreement with the average of MAMI, JLab/Hall-A, and CLAS experiments (with H. Atac, et al. (2021) fit [46]), and the world data (with Kelly (2004)

fit [47]), which is $\langle r_E^2 \rangle_n = (-0.110 \text{ fm}^2 - 0.112 \text{ fm}^2)/2 = -0.111 \text{ fm}^2$.

We have summarized our result for the electromagnetic radii of the proton and neutron in Table II.

Nucleon radii	Experimental values	Soft-wall AdS/QCD [This work]
$\sqrt{\langle r_M^p \rangle^2}$	0.822 fm (e-p world average)	$0.803 \pm 0.012 \text{ fm}$ (extracted)
$\sqrt{\langle r_C^p \rangle^2}$	0.831 fm (PRad 2019)	$0.831 \pm 0.008 \text{ fm}$ (predicted)
$\sqrt{\langle r_C^p \rangle^2}$	0.841 fm (μp Lamb shift)	$0.831 \pm 0.008 \text{ fm}$ (predicted)
$\sqrt{\langle r_M^n \rangle^2}$	0.864 fm (PDG world average)	$0.817 \pm 0.007 \text{ fm}$ (predicted)
$\langle (r_C^n)^2 \rangle$	-0.111 fm ² (world average)	$-0.094 \pm 0.048 \text{ fm}^2$ (predicted)

TABLE II: Comparison of the soft-wall holographic QCD electromagnetic radii of the proton and neutron with experiment. See text for the references of the quoted experimental values.

V. CONCLUSIONS

By fixing the twist parameter of the nucleon $\tau = 3$, and $\kappa = 0.402 \text{ GeV}$, we have found a much improved description of the world data (including the Mainz A1 [6], Jefferson Lab recoil polarization experiment E08-007 [30], and PRad data [11]), of both the electric and magnetic Sachs form factors (including their ratio) of the proton. The agreement with the data range from low to high momentum transfers, all within the original-minimal soft-wall holographic QCD [25, 26], see Figs. 2-4. For example, from our electric Sachs form factor of the proton (II.1), we have found the charge radius of the proton to be $r_p = 0.831 \pm 0.008 \text{ fm}$ in perfect agreement with the recent charge radius of the proton measured by the PRad collaboration at Jefferson Lab [11]. Our theoretical error in the charge radius of the proton, stems from our alternative choice of $\tau = m_N^2/m_\rho^2 + 1 = 2.465$, and $\kappa = m_\rho/2 = 0.388 \text{ GeV}$, which gives the charge radius of proton to be $r_p = 0.839 \text{ fm}$, see Table I.

To our knowledge, our holographic framework is the only theoretical work that produces a perfect match to the recent PRad collaboration measurement of the charge radius of the proton. We have also computed the charge and magnetic radii of the neutron, as well as the magnetic radius of the proton, with a good agreement to the experimental values, see Table II. This is not surprising given the non-perturbative nature of the problem, and the phenomenological success of the original soft-wall holographic QCD construction [25, 26, 40, 48–55],

with only three parameters: the mass scale κ , the twist parameter of the nucleon τ , and the 't Hooft coupling constant λ (also needed for high energy t-channel diffractive processes).

Holography recovers the old dual description with all its phenomenological successes. As we noted earlier, it is the most economical way of enforcing QCD symmetries, duality and crossing symmetries, all usually sought by dispersive analyses, and yet within a well defined and minimal organisational principle using field theory. The present analyses and results are an illustration of that.

However, holography provides much more. Indeed, the bulk holographic description in higher dimension allows for the assessment of any n-point function on the boundary, using field theoretical methods through dual Witten diagrams, in the double limit of large N_c and strong gauge coupling. It is the QCD string made user friendly. It also provides for novel physics for processes at low parton-x [53], and for scattering on dense systems as dual to black holes [56, 57].

Acknowledgments

K.M. is supported by the U.S. Department of Energy, Office of Science, Office of Nuclear Physics, contract no. DE-AC02-06CH11357, and an LDRD initiative at Argonne National Laboratory under Project No. 2020-0020. I.Z. is supported by the Office of Science, U.S. Department of Energy under Contract No. DE-FG-88ER40388.

Appendix A: Soft-wall holographic QCD

A simple way to capture AdS/CFT duality in the non-conformal limit is to model it using a slice of AdS_5 with various bulk fields with assigned anomalous dimensions and pertinent boundary values, in the so-called bottom-up approach which we will follow here using the conventions in our recent work in DIS scattering [52, 53]. We consider

AdS₅ with a soft wall with a background metric $g_{MN} = (\eta_{\mu\nu}, -1)R^2/z^2$ with the flat metric $\eta_{\mu\nu} = (1, -1, -1, -1)$ at the boundary. Confinement will be described by a harmonic background dilaton $\phi = \kappa^2 z^2$.

1. Bulk vector mesons

The vector mesons fields L, R are described by the bulk effective action [52, 58, 59]

$$S_M = -\frac{1}{4g_5^2} \int d^5x e^{-\phi(z)} \sqrt{g} g^{MP} g^{NQ} \text{Tr} \left(\mathcal{F}_{MN}^L \mathcal{F}_{PQ}^L + \mathcal{F}_{MN}^R \mathcal{F}_{PQ}^R \right) + \int d^5x \left(\omega_5^L(\mathcal{A}) - \omega_5^R(\mathcal{A}) \right) \quad (\text{A.1})$$

with the Chern-Simons contribution

$$\omega_5(\mathcal{A}) = \frac{N_c}{24\pi^2} \int d^5x \text{Tr} \left(\mathcal{A} \mathcal{F}^2 + \frac{1}{2} \mathcal{A}^3 \mathcal{F} - \frac{1}{10} \mathcal{A}^5 \right) \quad (\text{A.2})$$

Here $\mathcal{F} = d\mathcal{A} - i\mathcal{A}^2$ and $\mathcal{A} = \mathcal{A}^a T^a$ with $T^0 = \frac{3}{2} \mathbf{1}_2$ and $T^i = \frac{1}{2} \tau^i$, with the form notation subsumed. Also the vector fields are given by $V = (R + L)/2$ and the axial-vector fields are given by $A = (R - L)/2$. The coupling g_5 in (A.1) is fixed by the brane embeddings in bulk, or phenomenologically as $1/g_5^2 \equiv N_c/(12\pi^2)$ [60].

The flavor gauge fields solve

$$\square V^\mu + z e^{\kappa^2 z^2} \partial_z \left(e^{-\kappa^2 z^2} \frac{1}{z} \partial_z V^\mu \right) = 0 \quad \square V_z - \partial_z \left(\partial_\mu V^\mu \right) = 0. \quad (\text{A.3})$$

subject to the gauge condition

$$\partial_\mu V^\mu + z e^{\kappa^2 z^2} \partial_z \left(e^{-\kappa^2 z^2} \frac{1}{z} V_z \right) = 0, \quad (\text{A.4})$$

with the boundary condition $V_\mu(z, y)|_{z \rightarrow 0} = \epsilon_\mu(q) e^{-iq \cdot y}$. The non-normalizable solutions are

$$\begin{aligned} V_\mu(z, y) &= \epsilon_\mu(q) e^{-iq \cdot y} \Gamma \left(1 - \frac{q^2}{4\kappa^2} \right) \kappa^2 z^2 \mathcal{U} \left(1 - \frac{q^2}{4\kappa^2}; 2; \kappa^2 z^2 \right) \\ V_z(z, y) &= \frac{i}{2} \epsilon(q) \cdot q e^{-iq \cdot y} \Gamma \left(1 - \frac{q^2}{4\kappa^2} \right) z \mathcal{U} \left(1 - \frac{q^2}{4\kappa^2}; 1; \kappa^2 z^2 \right), \end{aligned} \quad (\text{A.5})$$

with $\mathcal{U}(a; b; w)$ the confluent hypergeometric functions of the second kind.

The normalizable solutions (vector wavefunctions) are also given by [48]

$$\phi_n(z) = c_n \times \kappa^2 z^2 L_n^1(\kappa^2 z^2), \quad (\text{A.6})$$

with $c_n = \sqrt{2/n+1}$ which is determined from the normalization condition (for the soft-wall model with background dilaton $\phi = \kappa^2 z^2$)

$$\int dz \sqrt{g} e^{-\phi} (g^{xx})^2 \phi_n(z) \phi_m(z) = \delta_{nm}, \quad (\text{A.7})$$

Here $L_n^{(\alpha)}(\xi)$ are the generalized Laguerre polynomials. Therefore, we have

$$F_n = \frac{1}{g_5} \left(-e^{-\phi} \frac{1}{z'} \partial_{z'} \phi_n(z') \right)_{z'=\epsilon} = -\frac{2}{g_5} c_n (n+1) \kappa^2, \quad (\text{A.8})$$

with $\phi_n(z \rightarrow 0) \approx c_n \kappa^2 z^2 (n+1)$. Then, defining the decay constant as

$$f_n = -F_n/m_n,$$

we have

$$\phi_n(z) = \frac{f_n}{m_n} \times 2g_5 \times \kappa^2 z^2 L_n^1(\kappa^2 z^2), \quad (\text{A.9})$$

as required by vector meson dominance (VMD).

We can also write the non-normalizable solution as sum over the normalizable solutions as [48]

$$V(q, z) = \sum_n \frac{-g_5 F_n \phi_n(z)}{q^2 - m_n^2} = g_5^2 \times \sum_n \frac{f_n^2}{q^2 - m_n^2} \times 2\xi L_n^1(\xi), \quad (\text{A.10})$$

with $\xi = \kappa^2 z^2$.

2. Bulk Dirac fermions

The bulk Dirac fermion action in a sliced of AdS_5 is

$$S_F = \frac{1}{2g_5^2} \int d^5x e^{-\phi(z)} \sqrt{g} \left(\mathcal{L}_{F1} + \mathcal{L}_{F2} \right) + \frac{1}{2g_5^2} \int d^4x \sqrt{-g^{(4)}} \left(\mathcal{L}_{UV1} + \mathcal{L}_{UV2} \right), \quad (\text{A.11})$$

The Dirac and Pauli contributions to $\mathcal{L}_{F1,2}$ are respectively

$$\begin{aligned} \mathcal{L}_{\text{Dirac}1,2} &= \left(\frac{i}{2} \bar{\Psi}_{1,2} e_A^N \Gamma^A (\vec{D}_N^{L,R} - \overleftarrow{D}_N^{L,R}) \Psi_{1,2} - (\pm M + V(z)) \bar{\Psi}_{1,2} \Psi_{1,2} \right), \\ \mathcal{L}_{\text{Pauli}1,2} &= \pm 2g_5^2 \times \eta \bar{\Psi}_{1,2} e_A^M e_B^N \sigma^{AB} \mathcal{F}_{MN}^{L,R} \Psi_{1,2}, \end{aligned} \quad (\text{A.12})$$

with $V(z) = \kappa^2 z^2$, $e_A^N = z \delta_A^N$, $\sigma^{AB} = \frac{i}{2} [\Gamma^A, \Gamma^B]$, and $\omega_{\mu z \nu} = -\omega_{\mu \nu z} = \frac{1}{z} \eta_{\mu \nu}$. The Dirac gamma matrices $\Gamma^A = (\gamma^\mu, -i\gamma^5)$ are chosen in the chiral representation. They satisfy the flat anti-commutation relation $\{\Gamma^A, \Gamma^B\} = 2\eta^{AB}$. The left and right covariant derivatives are defined as

$$\begin{aligned} \vec{D}_N^{X=L,R} &= \vec{\partial}_N + \frac{1}{8} \omega_{NAB} [\Gamma^A, \Gamma^B] - i X_N^a T^a \equiv \vec{\mathcal{D}}_N - i X_N^a T^a \\ \overleftarrow{D}_N^{X=L,R} &= \overleftarrow{\partial}_N + \frac{1}{8} \omega_{NAB} [\Gamma^A, \Gamma^B] + i X_N^a T^a \equiv \overleftarrow{\mathcal{D}}_N + i X_N^a T^a \end{aligned} \quad (\text{A.13})$$

The nucleon doublet refers to

$$\Psi_{1,2} \equiv \begin{pmatrix} \Psi_{p1,2} \\ \Psi_{n1,2} \end{pmatrix}. \quad (\text{A.14})$$

The nucleon fields in bulk form an iso-doublet p, n with $1, 2$ referring to their boundary chirality $1, 2 = \pm = R, L$ [61]. They are dual to the boundary sources $\Psi_{p1,2} \leftrightarrow \mathcal{O}_{p,\pm}$ and $\Psi_{n1,2} \leftrightarrow \mathcal{O}_{n,\pm}$ with anomalous dimensions $\pm M = \pm(\Delta - 2) = \pm(\tau - 3/2)$.

The equation of motions for the bulk Dirac chiral doublet is

$$\left(i e_A^N \Gamma^A D_N^{L,R} - \frac{i}{2} (\partial_N \phi) e_A^N \Gamma^A - (\pm M + V(z)) \right) \Psi_{1,2} = 0, \quad (\text{A.15})$$

The normalizable solution to (A.15) are

$$\begin{aligned}\Psi_1(p, z) &= \psi_R(z)\Psi_R^0(p) + \psi_L(z)\Psi_L^0(p) \\ \Psi_2(p, z) &= \psi_R(z)\Psi_L^0(p) + \psi_L(z)\Psi_R^0(p)\end{aligned}\quad (\text{A.16})$$

with the normalized bulk wave functions

$$\begin{aligned}\psi_R(z) &= \tilde{n}_R \xi^{\tau-\frac{3}{2}} L_n^{(\tau-2)}(\xi) = \frac{\tilde{n}_R}{\kappa^{\tau-2}} z^{\frac{5}{2}} \xi^{\frac{\tau-2}{2}} L_n^{(\tau-2)}(\xi), \\ \psi_L(z) &= \tilde{n}_L \xi^{\tau-1} L_n^{(\tau-1)}(\xi) = \frac{\tilde{n}_L}{\kappa^{\tau-1}} z^{\frac{5}{2}} \xi^{\frac{\tau-1}{2}} L_n^{(\tau-1)}(\xi),\end{aligned}\quad (\text{A.17})$$

Here $\xi = \kappa^2 z^2$, $L_n^{(\alpha)}(\xi)$, $\tilde{n}_R = \tilde{n}_L \kappa^{-1} \sqrt{\tau-1}$ are the generalized Laguerre, and $\tilde{n}_L = \kappa^\tau \sqrt{2/\Gamma(\tau)}$. The free Weyl spinors $\Psi_{R/L}^0(p) = P_\pm u(p)$ and $\bar{\Psi}_{R/L}^0(p) = \bar{u}(p) P_\mp$, and the free boundary spinors satisfy

$$\bar{u}(p)u(p) = 2m_N \quad 2m_N \times \bar{u}(p')\gamma^\mu u(p) = \bar{u}(p')[(p' + p)^\mu + i\sigma^{\mu\nu}(p' - p)_\nu]u(p). \quad (\text{A.18})$$

The fermionic spectrum Reggeizes $m_n^2 = 4\kappa^2(n + \tau - 1)$. The assignments $1 = +$ and $2 = -$ at the boundary are commensurate with the substitutions $\psi_{R,L} \leftrightarrow \mp \psi_{L,R}$ by parity.

Using the Dirac 1-form currents

$$\begin{aligned}J_L^{aN} &= \frac{\partial \mathcal{L}_{\text{Dirac}1}}{\partial L_N^a} = \bar{\Psi}_1 e_A^N \Gamma^A T^a \Psi_1, \\ J_R^{aN} &= \frac{\partial \mathcal{L}_{\text{Dirac}2}}{\partial R_N^a} = \bar{\Psi}_2 e_A^N \Gamma^A T^a \Psi_2,\end{aligned}\quad (\text{A.19})$$

and Pauli 2-form currents

$$\begin{aligned}J_L^{aMN} &= \frac{\partial \mathcal{L}_{\text{Pauli}1}}{\partial L_{MN}^a} = +2g_5^2 \times \eta^a \bar{\Psi}_1 e_A^M e_B^N \sigma^{AB} T^a \Psi_1, \\ J_R^{aMN} &= \frac{\partial \mathcal{L}_{\text{Pauli}2}}{\partial R_{MN}^a} = -2g_5^2 \times \eta^a \bar{\Psi}_2 e_A^M e_B^N \sigma^{AB} T^a \Psi_2.\end{aligned}\quad (\text{A.20})$$

we can rewrite (A.12) with the explicit isoscalar ($a = 0$) and isovector ($a = 3$) contributions

$$\begin{aligned}\mathcal{L}_{F1} + \mathcal{L}_{F2} \supset & \frac{i}{2} \bar{\Psi}_1 e_A^N \Gamma^A (\vec{\mathcal{D}}_N - \overleftarrow{\mathcal{D}}_N) \Psi_1 - (M + V(z)) \bar{\Psi}_1 \Psi_1 + \frac{i}{2} \bar{\Psi}_2 e_A^N \Gamma^A (\vec{\mathcal{D}}_N - \overleftarrow{\mathcal{D}}_N) \Psi_2 - (-M + V(z)) \bar{\Psi}_2 \Psi_2 \\ & + V_N^0 J_V^{0N} + A_N^0 J_A^{0N} + V_N^3 J_V^{3N} + A_N^3 J_A^{3N} + V_{MN}^0 J_V^{0MN} + A_{MN}^0 J_A^{0MN} + V_{MN}^3 J_V^{3MN} + A_{MN}^3 J_A^{3MN}\end{aligned}\quad (\text{A.21})$$

with $J_{V,A}^{aN} = J_L^{aN} \pm J_R^{aN}$ and $J_{V,A}^{aMN} = J_L^{aMN} \mp J_R^{aMN}$.

Appendix B: Electromagnetic form factors

The electromagnetic form factors for the nucleon in the context of the soft wall model have been originally addressed in [26], although with a different analysis at low momentum transfer than the one we will present and which will fix the numerical shortcomings they encountered. Holographic QCD maps gauge invariant operators

at the boundary with supergravity fields in bulk with pertinent anomalous dimensions. The bulk string theory is in general difficult to solve, but in the double limit of a large number of colors and strong gauge coupling $\lambda = g^2 N_c$, it reduces to a weakly coupled supergravity in the classical limit in AdS_5 geometry, with a weak string coupling $g_{string} = g^2/4\pi$. The n-point functions at the boundary of AdS_5 follow from variation of the on-shell

supergravity action in bulk with respect to the boundary values. The results are tree-level Feynman graphs with

fixed end-points on the boundary also known as Witten diagrams [62] (and references therein).

The electromagnetic form factor for the nucleon can be extracted from the normalized boundary-to-bulk Witten diagram for the 3-point function, with pertinent LSZ reduction

$$W_V^{a\mu}(q) = \lim_{p_2^2, p_1^2 \rightarrow m_N^2} (p_2^2 - m_N^2)(p_1^2 - m_N^2) \frac{\langle \mathcal{O}_N(-p_2) J_V^{a\mu}(q) \mathcal{O}_N(p_1) \rangle}{F_N(p_2) F_N(p_1)}, \quad (\text{B.1})$$

for the isoscalar $a = 0$ and the isovector $a = 3$ current $J_V^{a\mu}$. The nucleon source constant is $F_N(p) =$

$\langle 0 | \mathcal{O}_N(0) | N(p) \rangle$. The electromagnetic current form factors follow from the identification

$$\langle N(p_2) | J_{EM}^\mu(0) | N(p_1) \rangle = \bar{u}(p_2) \left(F_1(Q) \gamma^\mu + F_2(Q) \frac{i\sigma^{\mu\nu} q_\nu}{2m_n} \right) u(p_1) = \frac{1}{3} W_V^{0\mu}(Q^2) + W_V^{3\mu}(Q^2) = W_{EM}^\mu(Q^2) \quad (\text{B.2})$$

with $q^2 = (p_2 - p_1)^2 = -Q^2$ (space-like). Here $N(p)$ refers to the U(2) proton-neutron doublet.

The vector currents $J_V^{a\mu}$ at the boundary are sourced by the dual bulk vector fields $V_\mu^a(Q, z \rightarrow 0)$. The Dirac

and Pauli contributions to the direct part of the electromagnetic current can be extracted from the pertinent bulk Dirac and Pauli parts of the action in the soft wall model. The Dirac part of the action in (A.21) yields

$$\begin{aligned} S_{Dirac}^{EM}[i, f] &= \frac{1}{2g_5^2} \int dz d^4y \sqrt{g} e^{-\phi} \frac{z}{R} \\ &\times \left(\bar{\Psi}_{1f} \gamma^N \left(\frac{1}{3} V_N^0 T^0 + V_N^3 T^3 \right) \Psi_{1i} + \bar{\Psi}_{2f} \gamma^N \left(\frac{1}{3} V_N^0 T^0 + V_N^3 T^3 \right) \Psi_{2i} \right), \\ &= (2\pi)^4 \delta^4(p' - p - q) \times F_N(p') \times F_N(p) \\ &\times \frac{1}{2g_5^2} \times 2g_5^2 \times e_N \times \bar{u}_{sf}(p') \not{q} u_{si}(p) \times \frac{1}{2} \int \frac{dz}{z^{2M}} e^{-\phi} \mathcal{V}(Q, z) \left(\tilde{\psi}_L^2(z) + \tilde{\psi}_R^2(z) \right). \end{aligned} \quad (\text{B.3})$$

Here $M = \tau - \frac{3}{2}$, $\phi = \kappa^2 z^2$, and $\epsilon^\mu(q)$ is the polarization of the electromagnetic (EM) probe. In the last equality in (B.3), we substituted the bulk gauge fields by (A.5), and the bulk fermionic currents in terms of the fermionic fields (A.16). The charge assignments are $e_N = 1$ for the proton, and $e_N = 0$ for the neutron. We also use the nucleon (ground state) bulk wave functions given by (A.16)

$$\begin{aligned} \tilde{\psi}_R(z) &= n_R \xi^{\tau - \frac{3}{2}} L_0^{(\tau-2)}(\xi) \equiv n_R \xi^{\tau - \frac{3}{2}}, \\ \tilde{\psi}_L(z) &= n_L \xi^{\tau-1} L_0^{(\tau-1)}(\xi) \equiv n_L \xi^{\tau-1}, \end{aligned} \quad (\text{B.4})$$

with the generalized Laguerre polynomials $L_n^{(\alpha)}(\xi)$, $\xi = \kappa^2 z^2$, $n_R = n_L \sqrt{\tau-1}$ and $n_L = \kappa^{-(\tau-2)} \sqrt{2/\Gamma(\tau)}$. We also use the non-normalizable solution to the bulk U(1) gauge field (the bulk-to-boundary vector propagator) (A.5)

$$\mathcal{V}(Q, z) = g_5^2 \times \sum_n \frac{-f_n^2}{Q^2 + m_n^2} \times 2\xi L_n^1(\xi) = \xi \Gamma(1+a) \mathcal{U}(1+a; 2; \xi) = \xi \int_0^1 \frac{dx}{(1-x)^2} x^a \exp\left(-\frac{x\xi}{1-x}\right), \quad (\text{B.5})$$

with the decay constant of the vector meson resonances $f_n = \frac{\sqrt{2}\kappa}{g_5}$, linear Regge trajectory for mass of vector meson resonances $m_n^2 = 4\kappa^2(n+1)$, $a = Q^2/(4\kappa^2)$, and $\xi = \kappa^2 z^2$. The bulk-to-boundary propagator satisfies

$$\mathcal{V}(0, z) = \mathcal{V}(Q, 0) = 1.$$

The Dirac part of the electromagnetic current (B.2) follows from (B.3) by variation

$$W_{EM(Dirac)}^\mu(Q^2) = \bar{u}_{s'}(p') \gamma^\mu u_s(p) \times e_N \times C_1(Q) \equiv \frac{1}{F_N(p') F_N(p)} \frac{\delta S_{Dirac}^{EM}}{\delta \epsilon_\mu(q)} \quad (\text{B.6})$$

or more explicitly

$$\begin{aligned} C_1(Q) &= \frac{1}{2} \int \frac{dz}{z^{2M}} e^{-\phi} \mathcal{V}(Q, z) \left(\tilde{\psi}_L^2(z) + \tilde{\psi}_R^2(z) \right) = g_5^2 \times \sum_n \frac{-1}{Q^2 + m_n^2} \times \left[f_n^2 \int \frac{dz}{z^{2M}} e^{-\xi} \xi L_n^1(\xi) \left(\tilde{\psi}_L^2(z) + \tilde{\psi}_R^2(z) \right) \right], \\ &= g_5^2 \times \sum_n \frac{-1}{Q^2 + m_n^2} \times \mathcal{G}_{V_n \bar{B} B} = \int_0^1 dx \left(\tau \left(1 - \frac{x}{2} \right) - \frac{1}{2} \right) x^a (1-x)^{\tau-2} = \frac{(a+2\tau)\Gamma(a+1)\Gamma(\tau)}{2\Gamma(a+\tau+1)}, \\ &= \left(\frac{a}{2} + \tau \right) B(\tau, a+1), \end{aligned} \quad (\text{B.7})$$

where, in the last line, we have defined the Euler beta function $B(x, y) = \frac{\Gamma(x)\Gamma(y)}{\Gamma(x+y)}$. In the second line, we have also defined the vector meson resonances V_n coupling to the proton (baryon) B as

$$\mathcal{G}_{V_n \bar{B} B} \equiv f_n^2 \int \frac{dz}{z^{2M}} e^{-\xi} \xi L_n^1(\xi) \left(\tilde{\psi}_L^2(z) + \tilde{\psi}_R^2(z) \right), \quad (\text{B.8})$$

from which we can conclude that $\mathcal{G}_{V_n \bar{B} B} \sim N_c$, as expected in the large- N_c limit. Note that normalizing $C_1(0) = 1$ for the proton, fixes $1 + \mathcal{O}(N_c^{-2}) = 1$. The form factor readily crosses to time-like (modulo $1/N_c$ widths), with all meson-baryon-antibaryon couplings (B.8) fixed, in the double limit of large N_c and strong 't Hooft coupling! This clearly shows the relationship with constructions based on dispersive analyses [22] (and references therein).

The nucleon electromagnetic form factors including the Pauli contribution follows a similar reasoning, with the result for the proton

$$\begin{aligned} F_1^P(Q) &= C_1(Q) + \eta_P C_2(Q), \\ F_2^P(Q) &= \eta_P C_3(Q), \end{aligned} \quad (\text{B.9})$$

and the neutron

$$\begin{aligned} F_1^N(Q) &= \eta_N C_2(Q), \\ F_2^N(Q) &= \eta_N C_3(Q). \end{aligned} \quad (\text{B.10})$$

The additional invariant form factors stem from the Pauli contribution. They are structurally similar to the Dirac one in (B.7), with

$$\begin{aligned} C_2(Q) &= \frac{1}{2} \int \frac{dz}{z^{2M}} e^{-\phi} z \partial_z \mathcal{V}(Q, z) \left(\tilde{\psi}_L^2(z) - \tilde{\psi}_R^2(z) \right), \\ &= \int_0^1 dx \left(\tau x (\tau x + x - 3) + 1 \right) x^a (1-x)^{\tau-2}, \\ &= \frac{a(a(\tau-1)-1)\Gamma(a+1)\Gamma(\tau)}{\Gamma(a+\tau+2)}, \\ &= (\tau-1) \frac{a(a(\tau-1)-1)}{(a+\tau)(a+\tau+1)} B(\tau-1, a+1), \end{aligned} \quad (\text{B.11})$$

and

$$\begin{aligned}
C_3(Q) &= 2 \int \frac{dz}{z^{2M}} e^{-\phi} m_N z \mathcal{V}(Q, z) \tilde{\psi}_L(z) \tilde{\psi}_R(z), \\
&= \int_0^1 dx (4(\tau-1)\tau) x^a (1-x)^{\tau-1}, \\
&= \frac{4(\tau-1)\tau\Gamma(a+1)\Gamma(\tau)}{\Gamma(a+\tau+1)}, \\
&= 4(\tau-1)\tau B(\tau, a+1),
\end{aligned} \tag{B.12}$$

with $m_N^2 = 4\kappa^2(\tau-1)$. Note that the contributions $C_{1,2}(Q)$ to the Dirac form factors are chirality-spin preserving with LL and RR following the γ^μ assignment, while the contribution $C_3(Q)$ to the Pauli form factor is chirality-spin flipping with LR following the $\sigma^{\mu\nu}$ assignment.

Appendix C: Hard scattering rule and the dual resonance model

The hard scaling behavior for the electric form factor [39] is recovered at high energy by fixing $\tau \rightarrow 3$. Indeed, the contribution $C_1(Q)$ to the Dirac form factor $F_1(Q)$ in (B.7) with $a \gg 1$ and fixed τ , asymptotes

$$C_1(Q) = \left(\frac{a}{2} + \tau\right) \times B(\tau, a+1) \approx \frac{1}{2} \frac{\Gamma(\tau)}{a^{\tau-1}}, \tag{C.1}$$

in agreement with the hard scattering rule for $\tau = 3$. Similarly, the Pauli contribution $C_2(Q)$ to the Dirac form factor $F_1(Q)$ in (B.11), at high momentum with $a \gg 1$ and fixed τ , asymptotes

$$\begin{aligned}
C_2(Q) &= (\tau-1) \frac{a(a(\tau-1)-1)}{(a+\tau)(a+\tau+1)} B(\tau-1, a+1), \\
&\approx (\tau-1) \frac{\Gamma(\tau)}{a^{\tau-1}},
\end{aligned} \tag{C.2}$$

also in agreement with the hard scattering rule for $\tau = 3$. Note that The Pauli term contribution $C_3(Q)$ to the Pauli

form factor $F_2(Q)$ in (B.12), at high momentum with $a \gg 1$ and fixed τ , asymptotes to

$$C_3(Q) = 4\tau(\tau-1)B(\tau, a+1) \approx 4\tau(\tau-1) \frac{\Gamma(\tau)}{a^\tau}, \tag{C.3}$$

which is subleading in $1/Q^2$.

This scaling law originates from the contribution of the R-spinor (B.4) in the form factor near the UV boundary, as it dwarfs that of the L-spinor (B.4) when inserted in the integral (B.7), with the bulk-to-boundary propagator $\mathcal{V}(Q, z \sim 1/Q) \approx 1$. More specifically, the integrand in (B.7) gives

$$\left(\frac{z}{z^{2M}}\right) \times \xi^{2\tau-3}(1+\xi) \approx \frac{z^{4\tau-6}}{z^{2\tau-4}} \approx \left(\frac{1}{Q^2}\right)^{\tau-1} \tag{C.4}$$

Note that the Pauli contributions in (B.11) carry integrands with extra $z \sim 1/Q$ suppression near the UV boundary, and are sub leading in $1/Q^2$. This is expected since the Pauli term is helicity-flipping.

Finally, we note the close relationship between the nucleon form factor obtained in the old resonance dual model [35]

$$\frac{B(r_V, \frac{1}{2} + a)}{B(r_V, \frac{1}{2})} \tag{C.5}$$

and the holographic form factors (C.1-C.3). In (C.5), the spin rho Regge trajectory is

$$\frac{1}{2} + a = \frac{1}{2} + \alpha' t,$$

with $r_V = \tau - 1$ and $\alpha' = 1/4\kappa^2$ the open string or rho meson Regge slope. Since the dual resonance description is rooted in the Veneziano amplitude for open string scattering, it is not surprising that the holographic description which captures the dominant stringy excitations in bulk, yields similar results.

-
- [1] C. E. Carlson, Prog. Part. Nucl. Phys. **82**, 59 (2015), 1502.05314.
 - [2] J. C. Bernauer, EPJ Web Conf. **234**, 01001 (2020).
 - [3] H. Gao and M. Vanderhaeghen, Rev. Mod. Phys. **94**, 015002 (2022), 2105.00571.
 - [4] J. Arrington et al. (2021), 2112.00060.
 - [5] S. Durr et al., Science **322**, 1224 (2008), 0906.3599.
 - [6] J. C. Bernauer et al. (A1), Phys. Rev. Lett. **105**, 242001 (2010), 1007.5076.
 - [7] H. Fleurbaey, S. Galtier, S. Thomas, M. Bonnaud, L. Julien, F. Biraben, F. Nez, M. Abgrall, and J. Guéna, Phys. Rev. Lett. **120**, 183001 (2018), 1801.08816.
 - [8] A. Antognini et al., Science **339**, 417 (2013).
 - [9] N. Bezginov, T. Valdez, M. Horbatsch, A. Marsman, A. C. Vutha, and E. A. Hessels, Science **365**, 1007 (2019).
 - [10] A. Grinin et al., Science **370**, 1061 (2020).
 - [11] W. Xiong et al., Nature **575**, 147 (2019).
 - [12] T. Mart and A. Sulaksono, Phys. Rev. C **87**, 025807 (2013), 1302.6012.
 - [13] I. T. Lorenz and U.-G. Meißner, Phys. Lett. B **737**, 57 (2014), 1406.2962.
 - [14] K. Griffioen, C. Carlson, and S. Maddox, Phys. Rev. C **93**, 065207 (2016), 1509.06676.
 - [15] D. W. Higinbotham, A. A. Kabir, V. Lin, D. Meekins,

- B. Norum, and B. Sawatzky, Phys. Rev. C **93**, 055207 (2016), 1510.01293.
- [16] M. Horbatsch, E. A. Hessels, and A. Pineda, Phys. Rev. C **95**, 035203 (2017), 1610.09760.
- [17] S. Zhou, P. Giuliani, J. Piekarewicz, A. Bhattacharya, and D. Pati, Phys. Rev. C **99**, 055202 (2019), 1808.05977.
- [18] G. Lee, J. R. Arrington, and R. J. Hill, Phys. Rev. D **92**, 013013 (2015), 1505.01489.
- [19] A. V. Gramolin and R. L. Russell, Phys. Rev. D **105**, 054004 (2022), 2102.13022.
- [20] J. M. Alarcón, D. W. Higinbotham, and C. Weiss, Phys. Rev. C **102**, 035203 (2020), 2002.05167.
- [21] H. Atac, M. Constantinou, Z. E. Meziani, M. Paolone, and N. Sparveris, Eur. Phys. J. A **57**, 65 (2021), 2009.04357.
- [22] Y.-H. Lin, H.-W. Hammer, and U.-G. Meißner, Phys. Lett. B **816**, 136254 (2021), 2102.11642.
- [23] Z.-F. Cui, D. Binosi, C. D. Roberts, and S. M. Schmidt (2021), 2102.01180.
- [24] J. Zhou, V. Khachatryan, H. Gao, S. Gorbaty, and D. W. Higinbotham (2021), 2110.02557.
- [25] A. Karch, E. Katz, D. T. Son, and M. A. Stephanov, Phys. Rev. D **74**, 015005 (2006), hep-ph/0602229.
- [26] Z. Abidin and C. E. Carlson, Phys. Rev. D **79**, 115003 (2009), 0903.4818.
- [27] R. Pohl et al., Nature **466**, 213 (2010).
- [28] A. Beyer et al., Science **358**, 79 (2017).
- [29] P. J. Mohr, D. B. Newell, and B. N. Taylor, *CODATA recommended values of the fundamental physical constants: 2018*. (2019), URL <http://physics.nist.gov/constants>.
- [30] X. Zhan et al., Phys. Lett. B **705**, 59 (2011), 1102.0318.
- [31] P. J. Mohr, D. B. Newell, and B. N. Taylor, Journal of Physical and Chemical Reference Data **45**, 043102 (2016), URL <https://doi.org/10.1063/1.4954402>.
- [32] A. J. Krasznahorkay et al., Phys. Rev. Lett. **116**, 042501 (2016), 1504.01527.
- [33] C. E. Carlson and B. C. Rislow, Phys. Rev. D **86**, 035013 (2012), 1206.3587.
- [34] I. Zahed (2021), 2102.08191.
- [35] P. H. Frampton, Phys. Rev. D **1**, 3141 (1970).
- [36] J. M. Maldacena, Adv. Theor. Math. Phys. **2**, 231 (1998), hep-th/9711200.
- [37] O. Aharony, S. S. Gubser, J. M. Maldacena, H. Ooguri, and Y. Oz, Phys. Rept. **323**, 183 (2000), hep-th/9905111.
- [38] E. Witten, Adv. Theor. Math. Phys. **2**, 505 (1998), hep-th/9803131.
- [39] G. P. Lepage and S. J. Brodsky, Phys. Rev. D **22**, 2157 (1980).
- [40] A. Vega, I. Schmidt, T. Gutsche, and V. E. Lyubovitskij, Phys. Rev. D **83**, 036001 (2011), 1010.2815.
- [41] J. Arrington, W. Melnitchouk, and J. A. Tjon, Phys. Rev. C **76**, 035205 (2007), 0707.1861.
- [42] J. C. Bernauer et al. (A1), Phys. Rev. C **90**, 015206 (2014), 1307.6227.
- [43] M. Paolone et al., Phys. Rev. Lett. **105**, 072001 (2010), 1002.2188.
- [44] J. Arrington and I. Sick, J. Phys. Chem. Ref. Data **44**, 031204 (2015), 1505.02680.
- [45] P. A. Zyla et al. (Particle Data Group), PTEP **2020**, 083C01 (2020).
- [46] H. Atac, M. Constantinou, Z. E. Meziani, M. Paolone, and N. Sparveris, Nature Commun. **12**, 1759 (2021), 2103.10840.
- [47] J. J. Kelly, Phys. Rev. C **70**, 068202 (2004).
- [48] H. R. Grigoryan and A. V. Radyushkin, Phys. Rev. D **76**, 095007 (2007), 0706.1543.
- [49] P. Colangelo, F. De Fazio, F. Giannuzzi, F. Jugeau, and S. Nicotri, Phys. Rev. D **78**, 055009 (2008), 0807.1054.
- [50] H. Forkel, Phys. Rev. D **78**, 025001 (2008), 0711.1179.
- [51] N. R. F. Braga and A. Vega, Eur. Phys. J. C **72**, 2236 (2012), 1110.2548.
- [52] K. A. Mamo and I. Zahed, Phys. Rev. D **104**, 066010 (2021), 2102.00608.
- [53] K. A. Mamo and I. Zahed, Phys. Rev. D **101**, 086003 (2020), 1910.04707.
- [54] K. A. Mamo and I. Zahed, Phys. Rev. D **103**, 094010 (2021), 2103.03186.
- [55] K. A. Mamo and I. Zahed, Phys. Rev. D **104**, 066023 (2021), 2106.00722.
- [56] K. A. Mamo and I. Zahed, Phys. Rev. D **101**, 066013 (2020), 1807.07969.
- [57] K. A. Mamo and I. Zahed, Phys. Rev. D **101**, 066014 (2020), 1905.07864.
- [58] J. Hirn and V. Sanz, JHEP **12**, 030 (2005), hep-ph/0507049.
- [59] S. K. Domokos, H. R. Grigoryan, and J. A. Harvey, Phys. Rev. D **80**, 115018 (2009), 0905.1949.
- [60] A. Cherman, T. D. Cohen, and E. S. Werbos, Phys. Rev. C **79**, 045203 (2009), 0804.1096.
- [61] D. K. Hong, T. Inami, and H.-U. Yee, Phys. Lett. B **646**, 165 (2007), hep-ph/0609270.
- [62] H. Nastase, *Introduction to the ADS/CFT Correspondence* (Cambridge University Press, 2015), ISBN 978-1-107-08585-5, 978-1-316-35530-5.